ADVANCED OPTICAL MATERIALS
www.advopticalmat.de

Near-Infrared Reflection Modulation Through Electrical Tuning of Hybrid Graphene Metasurfaces

*Ziqiang Cai and Yongmin Liu**

Graphene, a 2D material with tunable optical properties, has recently attracted intense interest for reconfigurable metasurfaces. So far, the working wavelength of graphene-based or hybrid graphene metasurfaces has been limited in the mid-infrared and terahertz spectra. In this paper, by combining graphene with Au nanostructures, the authors demonstrate a near-infrared tunable metasurface with decent modulation efficiency, weak dependence on graphene's carrier mobility, and small gate voltages, attributing to the unique interband transition of graphene. The experimental results agree well with numerical simulations. It is also shown that by properly designing the structural parameters of Au nanostructures, the hybrid graphene metasurface can be tunable in both near-infrared and mid-infrared regions.

1. Introduction

As the planar version of metamaterials, metasurfaces can control the amplitude, phase, polarization, and angular momentum of light by an array of subwavelength structures.[1–3] The field of metasurfaces has become one of the most promising frontiers in photonics due to the compact footprint and flexibility in light manipulation. To further advance the practical applications of metamaterials and metasurfaces, it is highly desirable to make them tunable or reconfigurable. People have demonstrated many tuning approaches through electrical, mechanical, optical, thermal, and chemical control over the geometries of the building blocks or intrinsic properties of the constituent materials.[4] Among all these tuning mechanisms, electrical tuning using graphene has the advantages of high tuning speed, high modulation efficiency, broadband tunable electro-optical properties, adaptability with silicon fabrication process as well as compactness,[5–13] showing great potential in numerous applications, including polarization tuning,[14,15] phase tuning,[16–18] photodetectors,[19–26] chemical sensing,[27,28] tunable lenses,[29–34] etc. On the other hand, graphene metasurfaces have the disadvantages of weak interaction with light due to graphene's atomically thin thickness, and the requirement of large gate voltage and high carrier mobility. Their working wavelengths are limited in mid-infrared and terahertz spectra. Tremendous efforts have been taken to overcome these problems over the past years. To enhance graphene's interaction strength with light, hybrid graphene metasurfaces, which incorporate metallic plasmonic structures, are used to increase the local field intensity in graphene, achieving modulation depth of more than 90% in reflection configuration[7,35] and more than 20% in transmission configuration.[36,37] The required gate voltage can be greatly reduced by combining a relatively thick amorphous silicon layer and a thin Al_2O_3 layer to replace the typical thick nonconductive dielectric layer, in which the amorphous silicon layer can provide necessary dielectric thickness for optical purpose and work as back-gate electrode at the same time.[38] In addition, by tailoring the structures to reach critical coupling between the radiation and graphene plasmonic modes, we can achieve large modulation depth even with low graphene carrier mobility.[35] Although these research efforts substantially advance the development of graphene metasurfaces, the working wavelength limit is still a major issue. There are some experimental works in which graphene metasurfaces can be modulated in the near-infrared or short wavelength region of mid-infrared, but they either utilize the extended interaction length provided by a waveguide or fiber,[39,40] or have some limitations including the low tuning range (reflectance change $\Delta R \leq 0.05$),[41,42] and the requirement of extremely high applied voltages (as large as 150 V) to mechanically move graphene flakes.[43,44]

In this paper, we report a tunable hybrid graphene metasurface design that can push the working wavelength into the near-infrared region (≤3.0 μm). The device combines metallic plasmonic structures with graphene to enhance the interband transition of graphene, resulting in decent tunability at near-infrared wavelengths. The applied voltage can be quite small due to the "step-like" change of graphene's conductivity. Moreover, since the interband transition of graphene is less sensitive to its carrier mobility, our device can work well with wet transferred chemical vapor deposition (CVD) graphene which has low carrier mobility. Therefore, the device has robust performance and holds the promise for large-area fabrication. Finally, by using anisotropic plasmonic structures, we demonstrate that our hybrid graphene metasurface can be tunable in either near-infrared or mid-infrared spectra, depending on the polarization

Z. Cai, Y. Liu
Department of Electrical and Computer Engineering
Northeastern University
Boston, MA 02115, USA
E-mail: y.liu@northeastern.edu
Y. Liu
Department of Mechanical and Industrial Engineering
Northeastern University
Boston, MA 02115, USA
The ORCID identification number(s) for the author(s) of this article can be found under https://doi.org/10.1002/adom.202102135.

DOI: 10.1002/adom.202102135

of input light. Our hybrid graphene metasurface shows the potential for many applications, including near-infrared electro-optic modulators, reconfigurable lenses, and polarization modulators.

2. Results and Discussions

The reason why most of the graphene metasurfaces are not tunable at short wavelengths can be explained by the optical property of graphene. **Figure 1**a plots the dispersive graphene's conductivity (σ) calculated by random phase approximation in the local limit (see the Experimental Section) when the Fermi energy (E_F) of graphene is 0.1 and 0.5 eV. The boundary between the near-infrared (blue region) and mid-infrared (red region) is 3 µm. The interaction between graphene and light has two contributions: interband transition and intraband transition.[6,45,46] Depending on the relationship between photon energy $\hbar\omega$ and twice the Fermi energy $2|E_F|$ (the $2|E_F|$ positions are marked as vertical black dashed lines in Figure 1a), graphene's optical properties are quite different.[47] When the photon energy is larger than twice the Fermi energy, that is, $\hbar\omega > 2|E_F|$, the interband transition dominates and graphene behaves like a semiconductor material. When $\hbar\omega < 2|E_F|$, intraband transition dominates and graphene behaves like a metallic material. In this case, graphene plasma can be generated, leading to strong light-graphene interaction.[6] As shown in Figure 1a, when $|E_F|$increases from 0.1 to 0.5 eV, the imaginary part of graphene conductivity (σ_i) greatly increases. Such a change gives rise to the significant resonance shift of graphene metasurface in the mid-infrared spectrum.[7,48–50] On the other hand, in the near-infrared region, the tuning of graphene's optical property is realized by the change of the real part of graphene conductivity (σ_r), which is around 60 µS. This change results in the slight amplitude tuning that has been observed at near-infrared wavelengths.[8,51] To make graphene behave as a metal in the near-infrared region, extremely high Fermi energy is required. However, the Fermi energy cannot exceed 0.6 eV in most practical situations.[29,35] Ion gel is able to provide around 1 eV Fermi energy,[49,52] but it has drawbacks like incompatibility with semiconductor fabrication process, unwanted fluctuations in the spectra due to Fabry–Perot resonance inside ion gel,[41] and slow modulation speed arising from the long relaxation time of ions.[53,54]

To improve the modulation efficiency at near-infrared region, we design a hybrid graphene metasurface structure, in which a plasmonic metasurface is combined with monolayer graphene to enhance the interaction between graphene and light. Figure 1b schematically shows the unit cell of our hybrid graphene metasurface. The top metasurface and back reflector are made of Au, and the Al_2O_3 spacer layer is fabricated by atomic layer deposition (ALD). Monolayer graphene is placed underneath the top Au metasurface. When light is normally incident on the metasurface with the electric field polarized along the

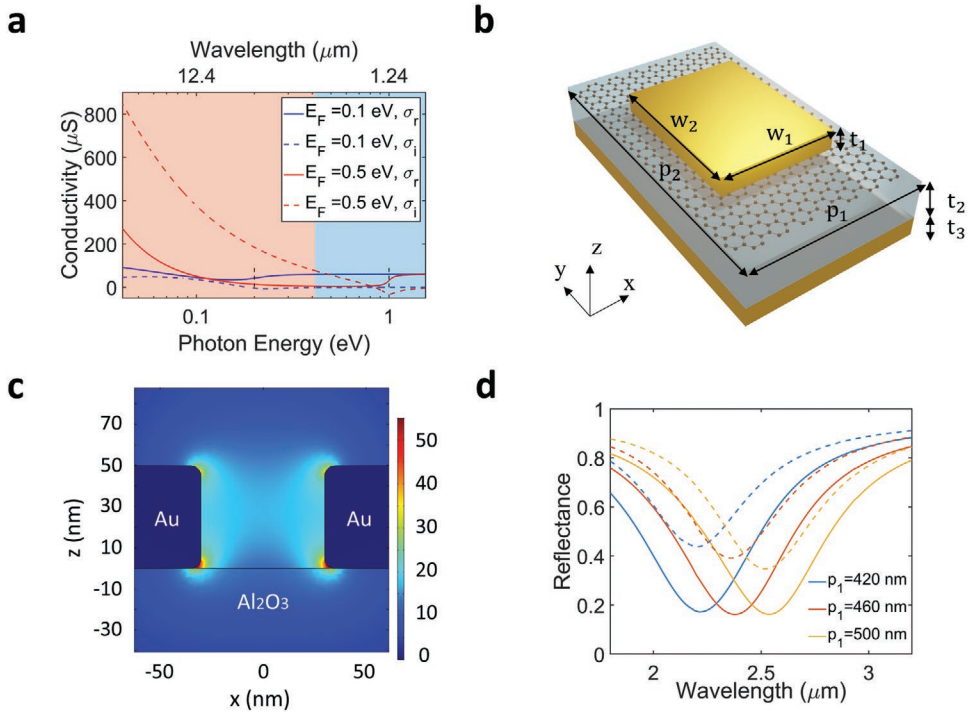

Figure 1. a) Spectra of the complex surface conductivity (σ) of graphene at different Fermi energies. The solid and dashed curves show the real (σ_r) and imaginary (σ_i) part of the conductivity, respectively. The mid-infrared spectral range is marked in red and the near-infrared spectral range is marked in blue. b) Schematic of the unit cell of the proposed hybrid graphene metasurface. It is composed of a gold back-reflector (t_3 = 50 nm), an Al_2O_3 layer (t_2 = 100 nm) and an Au resonator (t_1 = 50 nm, w_1 = 400 nm, w_2 = 540 nm) on top of monolayer graphene. The periodicity along the *x*- and *y*-axis is p_1 = 460 nm and p_2 = 1000 nm, respectively. c) Distribution of normalized electric field ($|E|/|E_0|$) in the *x*–*z* plane when a TM polarized (electric field is *x*-polarized) wave is perpendicularly incident on the metasurface. d) Simulated reflection spectra of metasurfaces with monolayer graphene (solid lines) and without graphene (dashed lines) when p_1 is varied.

x-direction, the light can be concentrated within the narrow gap between the Au meta-atoms, which greatly enhances the field intensity in the gap due to the plasmonic resonance. For the simulation results in this paper, if not otherwise stated, the mobility of graphene is 200 cm^2 $(V\ s)^{-1}$, and the Fermi energy of graphene is 0.25 eV for zero gate voltage (V_g), which are from the experimental characterization of graphene (see Section S1 in the Supporting Information). Figure 1c shows the electric field distribution inside the gap. A rounded corner with 5 nm radius is considered in this simulation. As can be seen, the highest intensity is around the corner of the Au resonators. Therefore, to increase the graphene-light interaction, graphene needs to have a good contact with these corners. For this reason, unlike some graphene metasurfaces that work in the mid-infrared,[18,37] O_2 plasma etching is not allowed between e-beam lithography of metasurface patterns and Au deposition, because this process can leave tiny gaps between the Au resonators and graphene (see Section S2 of the Supporting Information for more details). The simulated reflection spectra of the metasurfaces with and without graphene are plotted in Figure 1d. In the simulation, the periodicity of the metasurface along the *x*-axis is varied (420, 460, and 500 nm), and that along the *y*-axis is fixed (1000 nm). From this figure, we can see that a given metasurface with and without graphene shows the spectral resonance at very similar wavelength, while the metasurface with graphene has lower reflectance due to the additional absorption from graphene. This feature is different from the counterparts working in the mid-infrared and terahertz regions, where graphene substantially changes the resonant wavelength of the metallic metasurfaces.[35,37]

The simulated tuning performance of the hybrid graphene metasurface is demonstrated in **Figure 2**. When the gate voltage V_g is applied across the Al_2O_3 spacing layer between graphene and the bottom Au back reflector, the carrier concentration in graphene will be changed accordingly, which leads to the modulation in the reflectance. Figure 2a shows the tuning of the metasurface reflection spectra by the applied voltage (anode applied on the Au back reflector). The change of carrier concentration in graphene Δn can be estimated by a simple capacitor model, that is, $\Delta n = -C_g \cdot V_g/e$. Here $C_g = 8.06 \times 10^{-4}$ F m^{-2}, which is the capacitance per unit area of the dielectric layer, e is the electron charge, and the sign of Δn accounts for the doping type (that is, positive/negative Δn represents hole/electron doping). For each V_g, the corresponding E_F can be calculated by the equation: $E_F = \hbar v_F \sqrt{\pi |n|} = \hbar v_F \sqrt{\pi |n_0 + \Delta n|}$, where $\hbar$ is the Planck constant, v_F is the Fermi velocity of graphene, and $n_0 = 4.6 \times 10^{12}$ cm^{-2}, which is the carrier concentration at zero gate voltage. Figure 2a shows the reflection spectra when V_g is tuned from −15 to 10 V. The corresponding E_F is varied from 0.4 to 0 eV. From Figure 2a, we can see that the tuning of graphene's carrier concentration mostly changes the amplitude of the reflection, with a slight change in the resonant

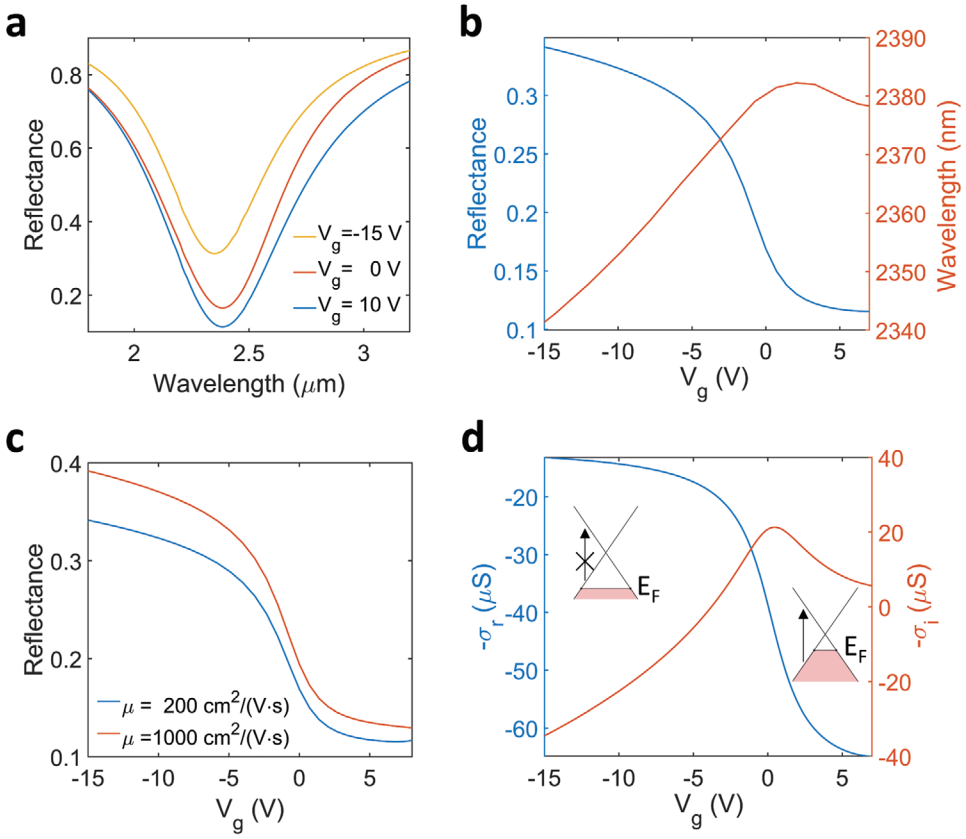

Figure 2. a) Simulated reflection spectra under different gate voltage V_g. b) Reflectance at 2.41 µm (blue curve) and resonant wavelength (red curve) for different V_g. c) Reflectance at 2.41 µm under different V_g and different mobilities. d) Real part (blue curve) and imaginary part (red curve) of graphene conductivity at 2.41 µm as a function of V_g. The insets show the schematic of graphene's electronic band structure.

wavelength. This is in sharp contrast to graphene metasurfaces that work at mid-infrared or terahertz frequencies,[7,18,55] which exhibit significant shift of the resonant wavelength. Figure 2b presents more details of the tuning process. The reflectance at 2.41 μm has a clear "step-like" change when V_g is tuned from + 5 to − 5 V, and slowly increases when V_g is below − 5 V. At the same time, the resonant wavelength (picked at the minimum in each reflectance spectrum) has a slight increase at the beginning, and then continuously decreases when V_g is tuned from + 5 to − 15 V. Compared with the amplitude variation, the resonant wavelength change (around 40 nm) is much less pronounced. Figure 2c shows the tuning of reflectance at 2.41 μm when graphene has different carrier mobilities. When the carrier mobility is 200 cm^2 $(V\ s)^{-1}$, the modulation of reflectance is $\Delta R = 0.223$, which is almost the same as the value $\Delta R = 0.260$ when the mobility is 5 times higher. This feature is notable. For most of the graphene metasurfaces that work in mid-infrared and terahertz spectra, the device performance highly depends on the carrier mobility of graphene, and even mechanical exfoliation is required in certain cases.[25,56,57] Our tunable metasurface, however, is insensitive to the carrier mobility of graphene, which relieves the requirement for graphene with high carrier mobilities.

The resonant frequency shift of graphene metasurfaces can be calculated according to $\Delta\omega_0 = \sigma_i \int |E_t|^2 \, dS / W_0$, where ω_0 is the resonant frequency, W_0 is the stored energy of the resonant mode, and E_t is the electric field component that is parallel to graphene surface.[50] The absorption in graphene is given by $A = \sigma_r \int 1/2 |E_t|^2 \, dS/P_0$, where P_0 is the incident power per unit area.[35] Therefore, the characteristic of the tuning process can be explained by the dependence of graphene's conductivity on the gate voltage. As shown in Figure 2d, the tuning process can be divided into three steps: (I) When $V_g > 5$ V, corresponding to $|E_F| < \hbar\omega/2$, graphene is semiconducting, and both real part and imaginary part of graphene's conductivity are almost constants. In this region, the interband transition dominates graphene's optical response, as can be seen in the inset on the right. (II) When V_g is tuned from 5 to −5 V, we approach the condition $|E_F| \approx \hbar\omega/2$. Graphene's interband transition is gradually suppressed due to Pauli blocking,[5] which prevents absorption in graphene and results in a "step" in the $-\sigma_r$ versus V_g curve. The $-\sigma_i$ curve, on the other hand, shows a first increase and then decrease feature. (III) When $V_g < -5$ V, corresponding to $|E_F| > \hbar\omega/2$, the interband transition is blocked, as shown in the inset on the left, and intraband transition starts to take over. Under this condition, σ_r is almost a constant, while $-\sigma_i$ continues to decrease. Since the absorption in graphene is proportional to σ_r, while the resonant frequency tuning is proportional to σ_i, Figure 2b,d follows a similar trend. The slow increase of reflection when $V_g < -5$ V, shown in Figure 2b, can be attributed to the slight blue-shift of the resonant wavelength. Although σ_r and σ_i have roughly the same amplitude of variation in Figure 2d, the wavelength tuning $\Delta\lambda \propto \Delta(1/\omega) \approx -\Delta\omega/\omega_0^2 \propto -\sigma_i/\omega_0^2$ is inversely proportional to the square of resonant frequency, resulting in a much smaller $\Delta\lambda$ at higher frequencies. From the above analysis, we can conclude that the reflection modulation mostly comes from the change in σ_r, which occurs within a small voltage window where Fermi energy is about half of the photon energy (i.e., $|E_F| \approx \hbar\omega/2$). Compared with other graphene metasurfaces that require large gate voltage tuning range ΔV_g to achieve large tuning in Fermi energy,[7,35,50] our graphene metasurface can greatly reduce the required voltage tuning range and hence benefit practical applications.

In our experiment, the voltage is applied between the electrode on top of the Al_2O_3 layer and the Au back reflector, as illustrated in **Figure 3**a. The scanning electron microscope (SEM) image of one fabricated metasurface is shown in Figure 3b. The reflectance spectra under different gate voltages are depicted in Figure 3c, which are measured by Fourier-transform infrared spectroscopy (FTIR). The clear change in the amplitude of reflectance agrees well with our simulation results (Figure 2a). Figure 3d depicts the amplitude change of reflection at 2.42 μm, where the largest modulation depth $\Delta R/R_{max}$ is achieved in our experiment. The resonant wavelength tuning is plotted in the same figure, which shows a small change around 25 nm. The "step-like" change in the reflection between −5 and +5 V, and the slight blue-shift of resonant wavelength at more negative voltage, agree well with the simulation result in Figure 2b. Due to the noise in the measurement data, the tiny resonant wavelength change cannot be precisely determined, causing fluctuations in the measured resonant wavelengths as shown in Figure 3d. However, the blueshift of the resonant wavelength can still be confirmed by comparing the measured spectra at +15 and −15 V. The details about resonant wavelength measurement are presented in Section S6 in the Supporting Information. The reflectance changes from 0.582 to 0.483, giving rise to a modulation depth of 17%. Although the key features of our experiment results are in accordance with simulation, the absolute values are quite different. More specifically, comparing the experiment result in Figure 3d with the simulation in Figure 2b, the measured reflectance modulation ΔR (0.10) is roughly half of the simulated ΔR (0.22), and the measured reflectance is much higher than simulation (hence much lower absorption in experiment). This large difference is likely a result of our defective fabrication process, which leaves a relatively thick layer of photoresist residue on top of the graphene surface, keeping graphene away from the hotspots at the corners of the Au meta-atoms. As we have mentioned earlier, the good contact between Au meta-atoms and graphene is critical for the tuning efficiency in our devices. The defects introduced during the fabrication compromise the experiment performance. After taking the photoresist residue layer into account in the simulation, we can get a better quantitative agreement between simulation and experiment. More details are given in Section S3 in the Supporting Information.

Another potential application is multi-wavelength tunable metasurface. Using anisotropic plasmonic structures, we can readily achieve resonant wavelengths in the near-infrared and mid-infrared for two orthogonal polarizations. Based on this idea, we have modified the metasurface geometry to the following: p_1 = 380 nm, p_2 = 1380 nm, w_1 = 320 nm, and w_2 = 1320 nm. **Figure 4**a shows the SEM picture of the fabricated metasurface. The measured reflection spectra under different voltages are presented in Figure 4b. The resonant wavelength is around 2.3 μm when electric field is x-polarized, and 6.0 μm when electric field is y-polarized. When the

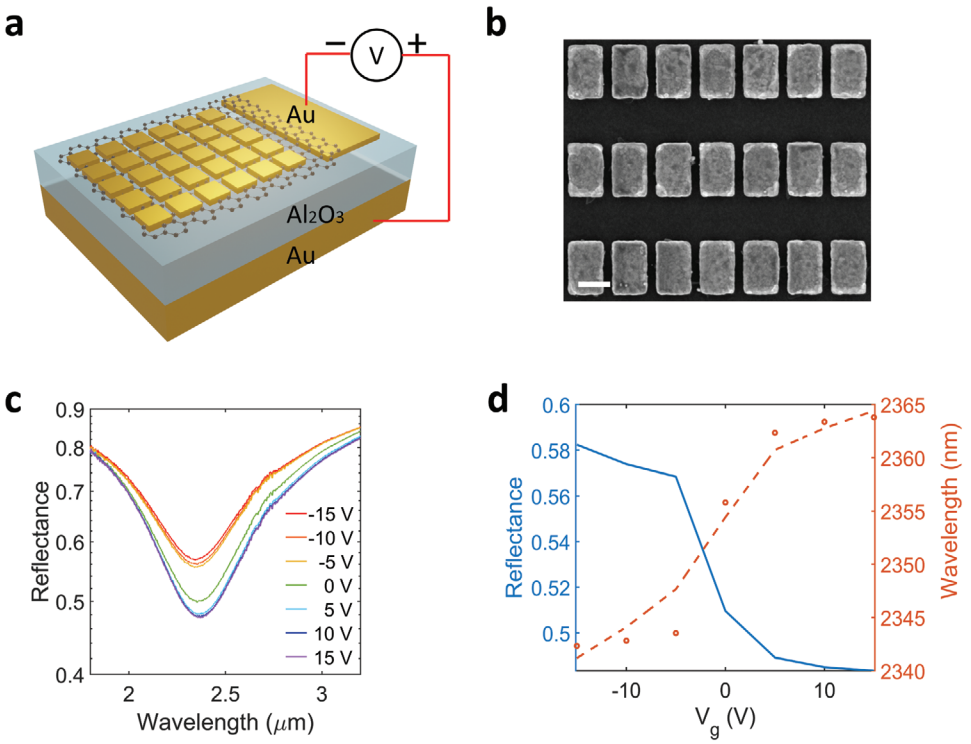

Figure 3. a) Schematic of the electrically tunable graphene metasurface. b) SEM image of the fabricated sample. The scale bar is 400 nm. c) Measured reflectance spectra of the metasurface with different gate voltages. The *y*-axis is in log scale. d) Measured reflectance at 2.42 μm (blue curve) and resonant wavelength (orange dots) under different gate voltages. The dashed line is guide for the eye.

gate voltage is tuned, the reflection spectra at *x*-polarization show an amplitude change in the near-infrared spectral range, while reflection spectra at *y*-polarization show a resonant wavelength shift in the mid-infrared spectral range. This is because graphene's optical property is dominated by graphene's interband transition and intraband transition in the near-infrared and mid-infrared regions, respectively. These features agree with the graphene optical characteristics illustrated in Figure 1a. The corresponding reflectance tuning at 2.30 and 5.67 μm are depicted in the experiment result shown in Figure 4c. When the input electric field is *x*-polarized, the measured reflectance changes from 0.522 to 0.427, giving rise to a modulation depth $\Delta R/R_{max}$ of 18.2% at 2.30 μm. When the input electric field is *y*-polarized, the measured reflectance changes from 0.229 to 0.304, giving rise to a modulation depth $\Delta R/R_{max}$ of 24.7% at 5.67 μm. Comparing the experiment result in Figure 4b with the simulation result in Figure 4d, we find good agreement between them. The quantitative difference can also be attributed to the imperfect fabrication. It should be noted that, due to the hysteresis feature of our graphene conductivity modulation (as shown in Figure S1 in the Supporting Information), for the same reflection spectra, the corresponding voltage in the experiment is not equal to the voltage in simulation. Furthermore, in the measured spectra in Figure 4b, there is an additional absorption peak around 2.7 μm for *y*-polarization, which is not present in Figure 4d. This absorption peak comes from the oblique angle of incidence during the measurement, as discussed in Section S4 in the Supporting Information.

Our graphene modulator has the optimal working wavelength at 2.42 μm. To achieve a shorter working wavelength, we shall decrease the resonant wavelength of the metasurface by changing its geometric parameters. Also, since most of the reflection tuning occurs at the transition wavelength $\hbar\omega \approx 2|E_F|$, shorter working wavelength requires larger $|E_F|$. $|E_F|$ can be increased by either applying a higher voltage or using chemical doping. It has been reported that by chemical doping, $|E_F|$ of the as-prepared CVD graphene can be increased from around 0.25 eV to over 0.40 eV,[55,58,59] corresponding to a transition wavelength from around 2.5 μm to less than 1.6 μm. If we do not use any chemical doping methods, the minimum achievable working wavelength depends on the maximum voltage that the device can sustain. If the applied voltage V_g is within the range from −20 to 5 V, the simulation results show that the hybrid graphene metasurface with modified geometry has a reflection change ΔR of 0.25 and a modulation depth of 47% at 2 μm. If the applied voltage can reach −50 V, approaching the breakdown limit of Al_2O_3 layer, then the working wavelength can be further decreased. Simulation results show that the hybrid graphene metasurface with proper geometry can achieve ΔR of 0.25 and modulation depth of 50% at 1.5 μm, as presented in Section S5 in the Supporting Information. However, due to the imperfection in fabrication, the quality of our ALD Al_2O_3 is relatively low, and our device suffers from the leakage current problem when the applied voltage is around −20 V. As a result, we cannot provide sufficient voltage bias for smaller working wavelength. Note that the highest breakdown electric field of ALD Al_2O_3 is experimentally

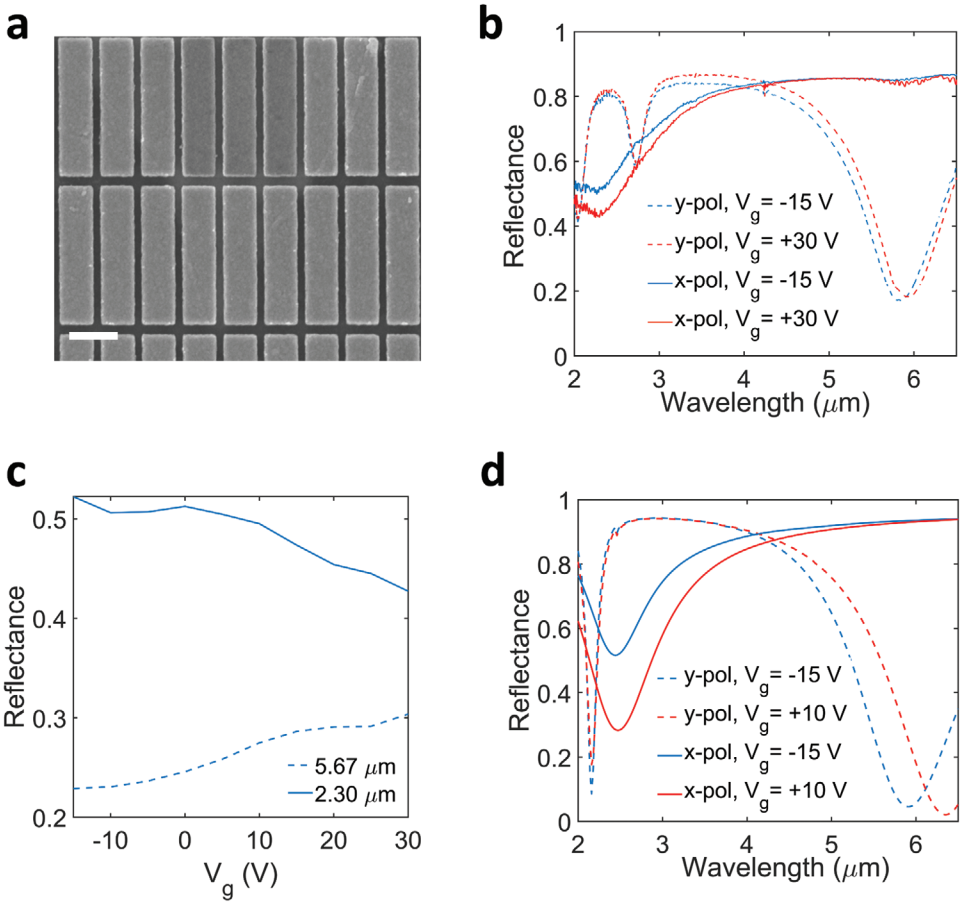

Figure 4. a) SEM image of the fabricated dual-wavelength graphene metasurface. The scale bar is 400 nm. b) Measured reflectance spectra of the graphene metasurface under different gate voltages when the input electric field is *x*-polarized (solid lines) and *y*-polarized (dashed lines). c) Measured reflectance at 2.30 and 5.67 μm under different gate voltages. d) Simulated reflectance spectra of the graphene metasurface.

reported to be 5–6 MV cm^{-1} elsewhere,[60] indicating a breakdown voltage of 50–60 V for 100 nm Al_2O_3 layer. Hence the working wavelength of our device could be further reduced by improving the fabrication process, such as cleaner surface before ALD process and rapid thermal annealing after deposition of Al_2O_3 layer.[61]

There has also been progress in using Indium Tin Oxide (ITO), a gate-tunable conducting oxide material, to make electronically tunable metasurface at near-infrared wavelengths.[60–62] When a gate voltage is applied, carrier concentration in ITO is redistributed, establishing an ultrathin accumulation layer near the interface between ITO and gate oxide. Under a proper gate voltage, epsilon-near-zero (ENZ) region can be formed in the accumulation layer, with a large electric field enhancement inside the ENZ region. The tunable metasurface based on ITO can achieve almost 2π phase tuning with a small amplitude change, making it possible for tunable beamsteering and focusing. However, the optical property of ITO layer highly depends on its growth condition, which must be carefully tuned so that ENZ region can be formed at the desired operating wavelength. Compared with the metasurfaces using ITO, graphene-based metasurfaces have a broader working wavelength range and a larger amplitude tuning range.

3. Conclusion

In summary, the working wavelengths of previously demonstrated graphene metasurfaces are largely limited in mid-infrared and terahertz spectra. In this work, utilizing graphene's interband transition, we have demonstrated a hybrid graphene metasurface that is tunable in the near-infrared region. Compared with the graphene metasurfaces that work at longer wavelengths, our metasurface has the advantages of insensitivity to graphene's carrier mobility, small voltage tuning range, and ultrathin thickness. The "step-like" modulation in the amplitude and the small resonant wavelength shift can be well explained by the characteristics of graphene's optical conductivity. The experiment results show a reflectance modulation ΔR of about 0.10 and a modulation depth $\Delta R/R_{max}$ of 17% at 2.42 μm, which are smaller than the simulated ΔR of 0.22 and $\Delta R/R_{max}$ of 66%. The quantitative difference between simulation and experiment results is attributed to the defective fabrication process. We have also designed and fabricated a hybrid graphene metasurface that can be tunable in either near-infrared or mid-infrared regions, depending on the polarization of the incident electric field. When light is at 2.30 μm and *x*-polarized, the measured ΔR is 0.095 and $\Delta R/R_{max}$ is 18.2%. When light is at 5.67 μm and *y*-polarized, the measured

ΔR is 0.075 and $\Delta R/R_{max}$ is 24.7%. The device performance can be further optimized by increasing the breakdown voltage of dielectric spacing layer,[61] applying double-layer graphene,[63] as well as improving the surface cleanliness of graphene through thermal annealing process.[64] Our hybrid graphene metasurfaces can be potentially applied in optical modulation, reconfigurable lenses, and polarization modulation in the infrared range.

4. Experimental Section

Numerical Simulation: The optical surface conductivity of graphene was calculated by random phase approximation[6,45–46]

$$\sigma(\omega)=\frac{i2e^2k_BT}{\pi^2(\omega+i\tau^{-1})}\ln\left[2\cosh\left(\frac{E_F}{2k_BT}\right)\right]+\frac{e^2}{4}\left[\frac{1}{2}+\frac{1}{\pi}\arctan\left(\frac{\omega-2E_F}{2k_BT}\right)-\frac{i}{2\pi}\ln\frac{(\omega+2E_F)^2}{(\omega-2E_F)^2+4(k_BT)^2}\right] \quad (1)$$

In this equation, k_B is the Boltzmann constant, T is the temperature, and τ^{-1} is the damping rate. The first term describes the optical response due to intraband transition, while the second term describes the optical response due to interband transition.

The whole structure was simulated by commercial software COMSOL Multiphysics, in which graphene is modeled using transition boundary condition.

Sample Fabrication: First, the 50-nm-thick Au back reflector pattern (500 μm × 500 μm square shape) was deposited on top of a Si wafer by photolithography and e-beam evaporation process. After cleaning the wafer by acetone and isopropanol, a layer of Al_2O_3 with 100 nm thickness was deposited using ALD process, followed by photolithography, e-beam evaporation and lift-off process to deposit Au electrodes. Next, after transferring the CVD-grown monolayer graphene (ACS Material, SKU#: CVCU1022) onto the substrate, photolithography and oxygen plasma etching were used to crop graphene into 500 μm × 500 μm patches, which overlapped with the Au back reflectors. Finally, the 50 nm Au resonators was fabricated by e-beam lithography, followed by the e-beam evaporation and lift-off process.

Supporting Information

Supporting Information is available from the Wiley Online Library or from the author.

Acknowledgements

Y.L. acknowledges the support of the Office of Naval Research (N00014-16-1-2409) and the National Science Foundation (DMR-1654192 and ECCS-2136168). The authors thank Yihao Xu for preparing the schematics in this paper.

Conflict of Interest

The authors declare no conflict of interest.

Data Availability Statement

The data that support the findings of this study are available from the corresponding author upon reasonable request.

Keywords

graphene, metasurfaces, modulation, near-infrared

Received: October 5, 2021
Revised: December 30, 2021
Published online: January 30, 2022

[1] N. Yu, F. Capasso, *Nat. Mater.* **2014**, *13*, 139.
[2] F. Ding, A. Pors, S. I. Bozhevolnyi, *Rep. Prog. Phys.* **2018**, *81*, 026401.
[3] Q. He, S. Sun, S. Xiao, L. Zhou, *Adv. Opt. Mater.* **2018**, *6*, 1800415.
[4] Q. He, S. Sun, L. Zhou, *Research* **2019**, *2019*, 1849272.
[5] A. N. Grigorenko, M. Polini, K. Novoselov, *Nat. Photonics* **2012**, *6*, 749.
[6] F. H. Koppens, D. E. Chang, F. J. Garcia de Abajo, *Nano Lett.* **2011**, *11*, 3370.
[7] Y. Yao, R. Shankar, M. A. Kats, Y. Song, J. Kong, M. Loncar, F. Capasso, *Nano Lett.* **2014**, *14*, 6526.
[8] M. S. Jang, V. W. Brar, M. C. Sherrott, J. J. Lopez, L. Kim, S. Kim, M. Choi, H. A. Atwater, *Phys. Rev. B* **2014**, *90*, 165409.
[9] A. Safaei, S. Chandra, M. N. Leuenberger, D. Chanda, *ACS Nano* **2019**, *13*, 421.
[10] D. C. Abeysinghe, N. Nader, J. Myers, J. R. Hendrickson, J. W. Cleary, D. E. Walker Jr, K.-H. Chen, Y. Liu, S. Mou, *J. Phys. Chem. C* **2019**, *123*, 19820.
[11] Z. Su, F. Cheng, L. Li, Y. Liu, *ACS Photonics* **2019**, *6*, 1947.
[12] Z. Huang, K. Yao, G. Su, W. Ma, L. Li, Y. Liu, P. Zhan, Z. Wang, *Opt. Lett.* **2018**, *43*, 2636.
[13] B. Liu, Y. Liu, S. Shen, *Phys. Rev. B* **2014**, *90*, 195411.
[14] S. Dutta-Gupta, N. Dabidian, I. Kholmanov, M. A. Belkin, G. Shvets, *Philos. Trans. R. Soc., A* **2017**, *375*, 20160061.
[15] J. Li, P. Yu, H. Cheng, W. Liu, Z. Li, B. Xie, S. Chen, J. Tian, *Adv. Opt. Mater.* **2016**, *4*, 91.
[16] N. Dabidian, S. Dutta-Gupta, I. Kholmanov, K. Lai, F. Lu, J. Lee, M. Jin, S. Trendafilov, A. Khanikaev, B. Fallahazad, E. Tutuc, M. A. Belkin, G. Shvets, *Nano Lett.* **2016**, *16*, 3607.
[17] Z. Miao, Q. Wu, X. Li, Q. He, K. Ding, Z. An, Y. Zhang, L. Zhou, *Phys. Rev. X* **2015**, *5*, 041027.
[18] M. C. Sherrott, P. W. C. Hon, K. T. Fountaine, J. C. Garcia, S. M. Ponti, V. W. Brar, L. A. Sweatlock, H. A. Atwater, *Nano Lett.* **2017**, *17*, 3027.
[19] D. Basko, *Science* **2011**, *334*, 610.
[20] M. Freitag, T. Low, W. Zhu, H. Yan, F. Xia, P. Avouris, *Nat. Commun.* **2013**, *4*, 1951.
[21] Z. Fang, Z. Liu, Y. Wang, P. M. Ajayan, P. Nordlander, N. J. Halas, *Nano Lett.* **2012**, *12*, 3808.
[22] T. J. Echtermeyer, S. Milana, U. Sassi, A. Eiden, M. Wu, E. Lidorikis, A. C. Ferrari, *Nano Lett.* **2016**, *16*, 8.
[23] S. Cakmakyapan, P. K. Lu, A. Navabi, M. Jarrahi, *Light: Sci. Appl.* **2018**, *7*, 20.
[24] Q. Guo, R. Yu, C. Li, S. Yuan, B. Deng, F. J. Garcia de Abajo, F. Xia, *Nat. Mater.* **2018**, *17*, 986.
[25] J. Wei, C. Xu, B. Dong, C.-W. Qiu, C. Lee, *Nat. Photonics* **2021**, *15*, 614.
[26] D. Wang, A. E. L. Allcca, T. F. Chung, A. V. Kildishev, Y. P. Chen, A. Boltasseva, V. M. Shalaev, *Light: Sci. Appl.* **2020**, *9*, 126.
[27] D. Rodrigo, O. Limaj, D. Janner, D. Etezadi, F. J. G. d. Abajo, V. Pruneri, H. Altug, *Science* **2015**, *349*, 165.
[28] H. Hu, X. Yang, X. Guo, K. Khaliji, S. R. Biswas, F. J. Garcia de Abajo, T. Low, Z. Sun, Q. Dai, *Nat. Commun.* **2019**, *10*, 1131.
[29] S. Han, S. Kim, S. Kim, T. Low, V. W. Brar, M. S. Jang, *ACS Nano* **2020**, *14*, 1166.
[30] S. Park, G. Lee, B. Park, Y. Seo, C. Bin Park, Y. T. Chun, C. Joo, J. Rho, J. M. Kim, J. Hone, S. C. Jun, *Light: Sci. Appl.* **2020**, *9*, 98.

[31] Z. Huang, B. Hu, W. Liu, J. Liu, Y. Wang, *J. Opt. Soc. Am. B* **2017**, *34*, 1848.
[32] Z. Li, K. Yao, F. Xia, S. Shen, J. Tian, Y. Liu, *Sci. Rep.* **2015**, *5*, 12423.
[33] T. T. Kim, H. Kim, M. Kenney, H. S. Park, H. D. Kim, B. Min, S. Zhang, *Adv. Opt. Mater.* **2018**, *6*, 1700507.
[34] W. Ma, Z. Huang, X. Bai, P. Zhan, Y. Liu, *ACS Photonics* **2017**, *4*, 1770.
[35] S. Kim, M. S. Jang, V. W. Brar, K. W. Mauser, L. Kim, H. A. Atwater, *Nano Lett.* **2018**, *18*, 971.
[36] S. Kim, M. S. Jang, V. W. Brar, Y. Tolstova, K. W. Mauser, H. A. Atwater, *Nat. Commun.* **2016**, *7*, 12323.
[37] Y. Xia, J. Wang, Y. Zhang, Y. Shan, Y. Dai, A. Chen, T. Shen, S. Wu, X. Liu, L. Shi, *Adv. Opt. Mater.* **2020**, *8*, 2000264.
[38] B. Zeng, Z. Huang, A. Singh, Y. Yao, A. K. Azad, A. D. Mohite, A. J. Taylor, D. R. Smith, H. T. Chen, *Light: Sci. Appl.* **2018**, *7*, 51.
[39] M. Liu, X. Yin, E. Ulin-Avila, B. Geng, T. Zentgraf, L. Ju, F. Wang, X. Zhang, *Nature* **2011**, *474*, 64.
[40] W. Li, B. Chen, C. Meng, W. Fang, Y. Xiao, X. Li, Z. Hu, Y. Xu, L. Tong, H. Wang, W. Liu, J. Bao, Y. R. Shen, *Nano Lett.* **2014**, *14*, 955.
[41] V. Thareja, J. H. Kang, H. Yuan, K. M. Milaninia, H. Y. Hwang, Y. Cui, P. G. Kik, M. L. Brongersma, *Nano Lett.* **2015**, *15*, 1570.
[42] N. K. Emani, T. F. Chung, A. V. Kildishev, V. M. Shalaev, Y. P. Chen, A. Boltasseva, *Nano Lett.* **2014**, *14*, 78.
[43] B. D. Thackray, P. A. Thomas, G. H. Auton, F. J. Rodriguez, O. P. Marshall, V. G. Kravets, A. N. Grigorenko, *Nano Lett.* **2015**, *15*, 3519.
[44] P. A. Thomas, O. P. Marshall, F. J. Rodriguez, G. H. Auton, V. G. Kravets, D. Kundys, Y. Su, A. N. Grigorenko, *Nat. Commun.* **2016**, *7*, 13590.
[45] Z. Cai, Y. Xu, C. Wang, Y. Liu, *Adv. Opt. Mater.* **2020**, *8*, 1901090.
[46] L. A. Falkovsky, *J. Phys.: Conf. Ser.* **2008**, *129*, 012004.
[47] K. Tielrooij, L. Orona, A. Ferrier, M. Badioli, G. Navickaite, S. Coop, S. Nanot, B. Kalinic, T. Cesca, L. Gaudreau, *Nat. Phys.* **2015**, *11*, 281.
[48] L. Ju, B. Geng, J. Horng, C. Girit, M. Martin, Z. Hao, H. A. Bechtel, X. Liang, A. Zettl, Y. R. Shen, F. Wang, *Nat. Nanotechnol.* **2011**, *6*, 630.
[49] Z. Fang, Y. Wang, A. E. Schlather, Z. Liu, P. M. Ajayan, F. J. de Abajo, P. Nordlander, X. Zhu, N. J. Halas, *Nano Lett.* **2014**, *14*, 299.
[50] N. Dabidian, I. Kholmanov, A. B. Khanikaev, K. Tatar, S. Trendafilov, S. H. Mousavi, C. Magnuson, R. S. Ruoff, G. Shvets, *ACS Photonics* **2015**, *2*, 216.
[51] N. K. Emani, T. F. Chung, X. Ni, A. V. Kildishev, Y. P. Chen, A. Boltasseva, *Nano Lett.* **2012**, *12*, 5202.
[52] F. Chen, Q. Qing, J. Xia, J. Li, N. Tao, *J. Am. Chem. Soc.* **2009**, *131*, 9908.
[53] H. Wang, Y. Wu, C. Cong, J. Shang, T. Yu, *ACS Nano* **2010**, *4*, 7221.
[54] J. Lee, M. J. Panzer, Y. He, T. P. Lodge, C. D. Frisbie, *J. Am. Chem. Soc.* **2007**, *129*, 4532.
[55] H. Yan, X. Li, B. Chandra, G. Tulevski, Y. Wu, M. Freitag, W. Zhu, P. Avouris, F. Xia, *Nat. Nanotechnol.* **2012**, *7*, 330.
[56] S. Dai, Q. Ma, M. K. Liu, T. Andersen, Z. Fei, M. D. Goldflam, M. Wagner, K. Watanabe, T. Taniguchi, M. Thiemens, F. Keilmann, G. C. Janssen, S. E. Zhu, P. Jarillo-Herrero, M. M. Fogler, D. N. Basov, *Nat. Nanotechnol.* **2015**, *10*, 682.
[57] G. X. Ni, A. S. McLeod, Z. Sun, L. Wang, L. Xiong, K. W. Post, S. S. Sunku, B. Y. Jiang, J. Hone, C. R. Dean, M. M. Fogler, D. N. Basov, *Nature* **2018**, *557*, 530.
[58] S. Bae, H. Kim, Y. Lee, X. Xu, J. S. Park, Y. Zheng, J. Balakrishnan, T. Lei, H. R. Kim, Y. I. Song, Y. J. Kim, K. S. Kim, B. Ozyilmaz, J. H. Ahn, B. H. Hong, S. Iijima, *Nat. Nanotechnol.* **2010**, *5*, 574.
[59] H. Yan, F. Xia, W. Zhu, M. Freitag, C. Dimitrakopoulos, A. A. Bol, G. Tulevski, P. Avouris, *ACS Nano* **2011**, *5*, 9854.
[60] Y. W. Huang, H. W. Lee, R. Sokhoyan, R. A. Pala, K. Thyagarajan, S. Han, D. P. Tsai, H. A. Atwater, *Nano Lett.* **2016**, *16*, 5319.
[61] G. Kafaie Shirmanesh, R. Sokhoyan, R. A. Pala, H. A. Atwater, *Nano Lett.* **2018**, *18*, 2957.
[62] G. K. Shirmanesh, R. Sokhoyan, P. C. Wu, H. A. Atwater, *ACS Nano* **2020**, *14*, 6912.
[63] D. Rodrigo, A. Tittl, O. Limaj, F. J. G. Abajo, V. Pruneri, H. Altug, *Light: Sci. Appl.* **2017**, *6*, e16277.
[64] Y. C. Lin, C. C. Lu, C. H. Yeh, C. Jin, K. Suenaga, P. W. Chiu, *Nano Lett.* **2012**, *12*, 414.